Flow past a rotating hydrophobic/nonhydrophobic circular cylinder in a flowing soap film

Navya Geethika Chikkam and Sanjay Kumar*
Department of Aerospace Engineering, Indian Institute of Technology, Kanpur, UP-208016, India

(Received 29 June 2019; published 25 November 2019)

Flow past a rotating cylinder of various surface characteristics is investigated experimentally in a flowing soap film of a soap film tunnel. Experiments are carried out at Reynolds numbers ∼200 and 250 with cylinders of different levels of hydrophobicity and normalized rotation rates (ratio of surface speed of cylinder to free-stream velocity) varying from 0 to 4.36. The diagnostic is done with flow visualization using interference technique, and quantitative measurements are obtained with particle image velocimetry. Global wake structure of a rotating hydrophobic/nonhydrophobic cylinder at various rotation rates is presented in this work. Reynolds number and hydrophobicity are found to have a substantial effect on the onset of the transition regime. Interestingly, the transition of von Kármán vortex shedding to single-signed vortex shedding occurred at a transition zone with no evidence of region of suppression in soap film tunnel experiments. The shed single-signed vortices at a rotation rate above the transition regime are of an opposite sense to the cylinder rotation direction. The experimental evidence of this new vortex shedding mode in a soap film tunnel is presented using flow visualization and particle image velocimetry. In addition, inequality in the shedding frequency of counterclockwise and clockwise vortices is observed whose value reaches maximum before the transition zone and then decreases. A higher rotation rate of 4.36 made the counterclockwise vorticity completely wrap around the cylinder at Reynolds number ∼250. Consequently, the stagnation point got lifted off from the surface at ∼135°. The relative circulation of shed clockwise vortices to counterclockwise vortices is observed to be increasing with rotation rate and reaches maximum at the transition zone. The variation of the Strouhal number with rotation rate for shed clockwise vortices is observed to be increasing until the transition regime, and subsequently it decreases. The Strouhal number for hydrophobic cylinders was found to be less compared to nonhydrophobic cylinder and was also observed to decrease with increase in hydrophobicity. The study of the far-wake structure shows the evidence of distortion in the wake structure due to the elongation of vortex pairs for both hydrophobic and nonhydrophobic cylinders.

DOI: 10.1103/PhysRevFluids.4.114802

I. INTRODUCTION

Flow past bluff bodies is a classic fluid dynamics problem involving interesting aspects like vortex shedding, flow separation, and many others. Flow past a circular cylinder is one example of such a problem which has been studied for more than a century. The flow results in alternate shedding of vortices from the cylinder surface depending on the flow velocity due to an adverse pressure gradient resulting in a Bénard von Kármán vortex street. These vortices are shed with a particular frequency termed nondimensionally as the Strouhal number, $\mathrm{St} = fD/U$, where f is

*skmr@iitk.ac.in

the vortex shedding frequency, D is the cylinder diameter, and U is the free-stream velocity. The flow finds applications in flow-induced oscillation problems. If the shedding frequency matches the natural frequency, the structure vibrates with larger amplitude due to resonance, which may result in structural failure. In addition, a low-pressure region is created behind the cylinder due to the formation of the wake, giving rise to pressure drag. This drag component is dependent on wake morphology, suggesting that wake modification can help in drag reduction.

Many significant efforts have been made towards wake modification of bluff bodies through forcing at the body surface. One such technique is rotating the surface, which was primarily a lift enhancement technique. Many inventions were made to utilize the lift generated by rotating cylinders. Flettner rotor ships, *the Buckau and the Barbara*, were built with an idea of replacing ship sails with rotors. Propulsion of these ships is due to lift generated by the Magnus effect. The Madaras rotor plant, patented in 1926, also used Magnus lift for power generation. One of the earliest experimental measurements by Prandtl [1] on rotating cylinders at various end conditions and aspect ratios stated that the maximum lift coefficient would be 4π at a velocity ratio of 4. In addition, at this condition stagnation points would coincide resulting in closed streamlines. Glauert [2] observed that Prandtl's limit can be exceeded and that the circulation increases indefinitely with α in the vortex suppression regime. Tokumaru and Dimotakis [3] observed that maximum lift obtained is greater than 4π (predicted by Prandtl [1]) and studied its dependence on aspect ratio and rotation rate.

Study of the high-alpha effect over the lift coefficient led to the discovery of a new mode of vortex shedding, which became an interesting area of research. Diaz *et al.* [4] found from his laboratory experiments that alternate vortex shedding activity disappears for $\alpha > 2$ for $\mathrm{Re} = 9000$, where α is the ratio of cylinder surface velocity to the free-stream velocity and Re is the Reynolds number based on the cylinder diameter. He also observed a qualitative change of flow around the cylinder with α. Modi [5] demonstrated that rotating cylinders are also for drag reduction and suppression of vortex-induced oscillations. Coutanceau *et al.* [6], from their experimental results, found that beyond a critical rotation rate α, only one vortex is formed for an impulsively started rotating and translating cylinder, and the critical rotation rate is about 2 at $\mathrm{Re} \leqslant 1000$, which is independent of the Re value. His results were supported by Badr *et al.* [7] with their numerical simulations. Badr *et al.* [8] subsequently investigated a Reynolds number range of 10^3 to 10^4 at $0.5 < \alpha < 3$ for an impulsively started rotating and translating cylinder and found an excellent agreement between the results obtained experimentally and theoretically, except at high rotation rates. Here vortex shedding is observed for low alpha ($\alpha < 3$). For higher alpha, experimental results showed that the flow becomes turbulent, whereas numerical simulations result in a steady state with no vortex shedding. Chen *et al.* [9] from their computations stated that for $\mathrm{Re} = 200$ and $\alpha \leqslant 3.25$, vortices are shed but are of weak strength. Later it was stated that erroneous results are obtained because of less computation time and corrected by Mittal *et al.* [10] by considering a larger timescale for computation. This was supported by experimental evidence of a new shedding mode by Kumar *et al.* [11]. Chew *et al.* [12] in his two-dimensional computations stated that the regime of suppression for $\mathrm{Re} = 1000$ occurs beyond $\alpha = 2$. From his observations, drag and lift coefficients approach asymptotic values at $\alpha \sim 2$. Kang *et al.* [13], from their numerical simulations, observed that the critical rotation rate varies logarithmically with Re in the range $60 < \mathrm{Re} < 160$, and it was observed that the St value remains almost constant with rotation rate. All previous works in this area show dissimilarity in the dependence of St with α. Diaz *et al.* [4], Kimura *et al.* [14], and Jaminet [15] showed the experimental evidence of an increase in St with α. Chew *et al.* [12] observed from his numerical investigation that the St value increases with α, whereas Kang *et al.* [13] and Hu *et al.* [16] stated that the St value decreases with α from their computations.

Rotation of a cylinder provides a very attractive way to control the flow with many beneficial effects. It would be interesting to see how the wake dynamics of a rotating cylinder can be manipulated by altering the cylinder surface characteristics, such as hydrophobicity. Hydrophobic surfaces have a special phenomenon of slippage of water from its surface which happens due to contact angle $>90^\circ$. It can be achieved either by chemical coating or by surface roughness or both. They were originally inspired by natural objects such as lotus leaves and other self-cleaning entities

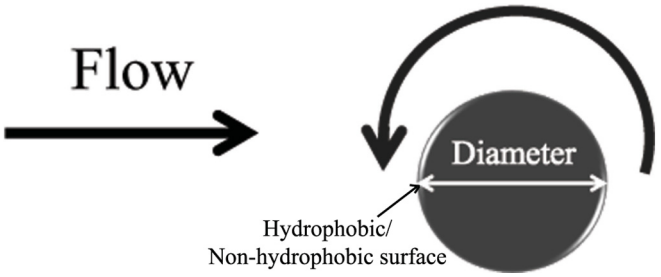

FIG. 1. Problem schematic showing rotating hydrophobic/nonhydrophobic cylinder of diameter, $D =$ 10 mm, rotating in a counterclockwise sense while viewing from the top.

in nature. Flow over the hydrophobic surface has been studied over the years both numerically and experimentally. Surface modification (hydrophobicity) has the advantage of controlling the wake structure as suggested by Muralidhar *et al.* [17]. Muralidhar *et al.* [17] found that superhydrophobic surfaces have a significant effect over the wake dynamics of the circular cylinder, mainly on the onset of vortex shedding. From their observations, it can be noted that superhydrophobic surfaces with ridges running normal to the flow cause the separation point to move downstream and the shedding frequency to increase with hydrophobic effect. In addition, the opposite trend is observed for both separation point and shedding frequency with ridges along the flow direction. Subsequently they observed a significant reduction in the drag for both laminar and turbulent flows. Min *et al.* [18] did numerical investigations with the main emphasis on the effect of hydrophobic surfaces on drag in channel flow. It was found that slip imparted in the streamwise direction decreases the skin-friction drag where spanwise slip increases the drag. You *et al.* [19] stated that slip condition enhances the flow instability, which in turn decreases the drag and rms lift coefficient around a circular cylinder at Re $=$ 300 and 3900. Ren *et al.* [20] in his recent studies showed the effect of superhydrophobic surfaces in flow past a rotating cylinder numerically at Re $=$ 100 in the range $\alpha = 0$ to 6 and stated that these surfaces can modify the critical rotation rates of vortex shedding. The behavior of hydrophobicity is inconsistent in a flow regime in terms of drag. In addition, he stated the trend of the Strouhal number to be increasing with hydrophobic effect. The problem of flow past a rotating cylinder with various degrees of hydrophobicity has not received attention to the best knowledge of the authors. The present work on the rotating cylinders was motivated by the desire to understand the effect of hydrophobicity on the wake structure of a rotating cylinder and to study the problem in a flowing soap film. The schematic of the problem is shown in Fig. 1. In addition, the present work investigates the downstream wake evolution up to $X \sim 85D$. This aspect of the wake was also studied by Taneda [21], Inoue *et al.* [22], and Georgiev *et al.* [23]. In particular Georgiev *et al.* [23] used particle image velocimetry (PIV) to understand the effect of the Reynolds number on the wake transition in a circular cylinder at Re ranging from 100 to 600. They observed an increase in wavelength after the wake transition. Flowing soap film offers the opportunity to study hydrodynamic phenomena in a two-dimensional scenario and has been widely used to study various hydrodynamic phenomena [24–29]. The main focus of the present work is to do the following:

(1) Study the global wake structure of a rotating cylinder in a two-dimensional soap film tunnel.

(2) Obtain the experimental evidence of the mode of vortex shedding at higher rotation rates.

(3) Study the effect of hydrophobicity of cylinder surface and Reynolds number over the onset of the new mode of vortex shedding and the global wake structure.

(4) Obtain far-wake morphology of the rotating cylinder (up to $X \sim 84D$ from the cylinder location).

To the best knowledge of the authors, there is no evidence of a similar experimental study. The present study was carried out at Re $\sim$200 and 250 and rotation rates ranging from 0 to 4.36 on rotating cylinders having surfaces with different levels of hydrophobicity. These values of Reynolds

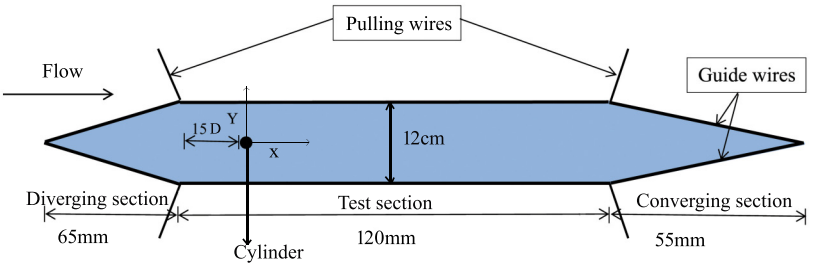

FIG. 2. Test section schematic.

numbers and rotation rates were chosen keeping the stability of film and limitation of rotation speed of the motor in consideration. The diagnostic is done using an interference-based flow visualization technique and quantitative measurements using the PIV technique.

II. EXPERIMENTAL SETUP AND DIAGNOSTICS

Rotating cylinders with different surface characteristics were studied in a gravity-driven inclined soap film tunnel. Figure 2 shows the details of the test section along with the converging and diverging sections. It consists of an inclined ($\sim$6.3°) test section of soap film having width $\sim$12 cm and length $\sim$120 cm. The thickness of the soap film averaged over various flow rates was approximately 7 μm. A soap solution of 2% by volume of surfactant (commercial Dettol dish wash liquid) in distilled water was used for this experiment. Here the top reservoir holds the soap solution and feeds it to the soap film continuously. The outlet of the top reservoir is connected to a crystal glass rotameter (Bimco. AB-786-MTR-CV) that measures the volume flow rate. A precision needle valve is attached to the rotameter to maintain the flow rate throughout the experiment. A metallic nozzle, connected to the outlet of rotameter, helps in guiding the soap solution to the guide wires (nylon wires $\sim$1 mm diameter). These wires are tied to the outlet of the metallic nozzle at one end and tensioned by dead weight at the other end. Another set of nylon wires ($\sim$0.8 mm diameter) are used as pulling wires to make the soap film of the desired width. These are attached to guide wires at four locations with a knot at one end and to PVC pipes at the other end. Both these type of wires provide a supportive structure to the soap film. A soap solution flowing between the guide wires is collected at the bottom end of guide wires using a bottom reservoir and recirculated through a pump to the top reservoir. The head of water in the top reservoir was maintained constant during the experiments.

In the soap film test section, the cylinder is placed at a distance of 15 cm from the starting point (end of diverging section). This cylinder is rotated by attaching it to low-rpm, high-torque 24 V DC motor from Bühler Motor Inc. (part no. 1.61.050.460.02). The rotation rate is referenced using a nondimensional rotation rate, α, which is the ratio of the surface velocity of the cylinder to the free-stream velocity of soap film in the tunnel test section. Surface velocity is a function of RPM of the motor, which varies with the supply voltage. RPM of the motor at various input voltage is measured using a noncontact tachometer, and the percentage of uncertainty in its measurement is 0.707%. The sense of rotation of the cylinder is set to be counterclockwise when viewed from the top.

A. Hydrophoic surfaces

In this work, flow past a rotating cylinder ($\sim$10 mm diameter) of various surface characteristics is studied. Surface characteristics imply imparting slip condition over the surface of the cylinder (i.e., hydrophobicity). These surfaces are inspired by a lotus leaf, where water slips off from its surface. This happens because of micro-nanostructured roughness over its surface, making it hydrophobic. In

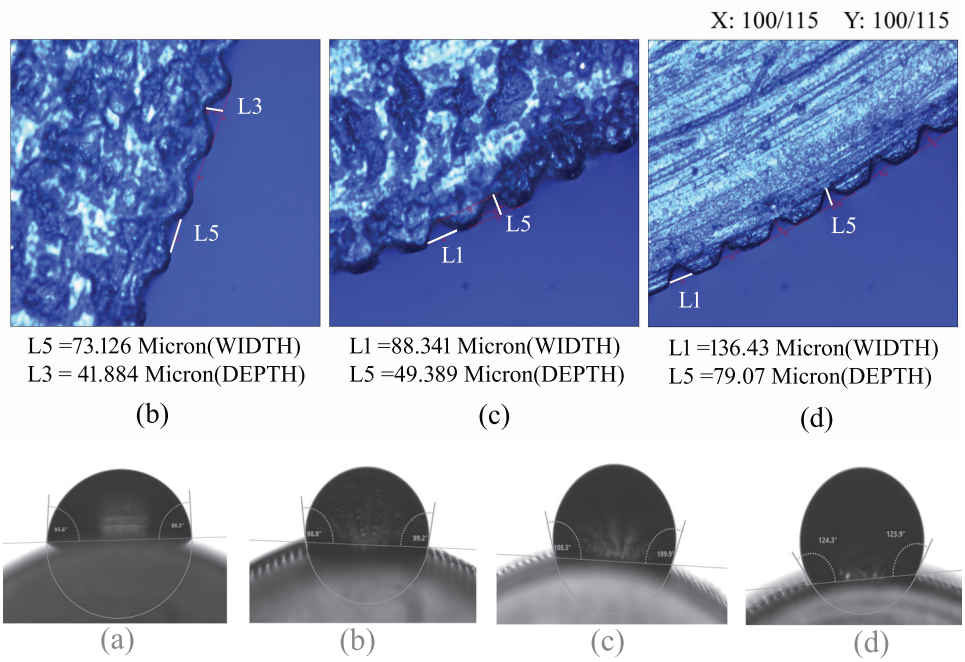

FIG. 3. (a) Nonhydrophobic cylinder, (b) hydrophobic cylinder of level I, (c) hydrophobic cylinder of level II, (d) hydrophobic cylinder of level III. (i) Dimensions of grooves over the various hydrophobic cylinders, (ii) contact angle made by various hydrophobic cylinders with water (a) 88.3°, (b) 99.2°, (c) 109.9°, (d) 123.9°.

general, cohesive forces dominate in a freely falling water droplet giving a spherical shape to water drop. But when it gets in contact with any surface, adhesive forces also come into picture resulting in wetting of the surface. But in hydrophobic surfaces, air gets trapped in the roughness over its surfaces and balances the weight of the water drop, resulting in the reduction of adhesive forces. This increases the contact angle, making water slip from the surface. A similar kind of surface is made with a machining process over the acrylic (plexiglass) cylinder. Three cylinders with different dimensions of grooves along the span [shown in Fig. 3(a)] over its surface were made using the Epilog laser engraving machining system (CO_2 laser). Figure 3(b) shows the section of a surface of a cylinder with three kinds of grooves giving three levels of hydrophobicity. A goniometry test showed that as the depth of groove increases, the contact angle made by water with the surface also increases, as shown in Fig. 3(b). In the present work, hydrophobicity is a surface characteristic defined with water as a reference medium (Fig. 3). This nature of the surface as depicted by contact angles shown in Fig. 3 could somewhat deviate for the dilute soap solution used in present study. The level of hydrophobicity is defined in terms of contact angle made by water with the surface. A surface making more contact angle with water has a high degree of hydrophobicity. Study of these surfaces for rotating cylinder experimentation is done individually.

In soap film tunnel experimentation, flow visualization and PIV are used to capture the flow behavior. The following sections describe our methodology.

B. Flow visualization

A soap film tunnel was equipped with a flow visualization technique based on light interference. For this study, a monochromatic light source (55W GE Low-pressure sodium vapor lamp) having a wavelength of 589.3 nm is incident on the soap film to create a constructive and destructive interference pattern [Fig. 4(a)]. Here a quarter of a wavelength change in thickness results in the

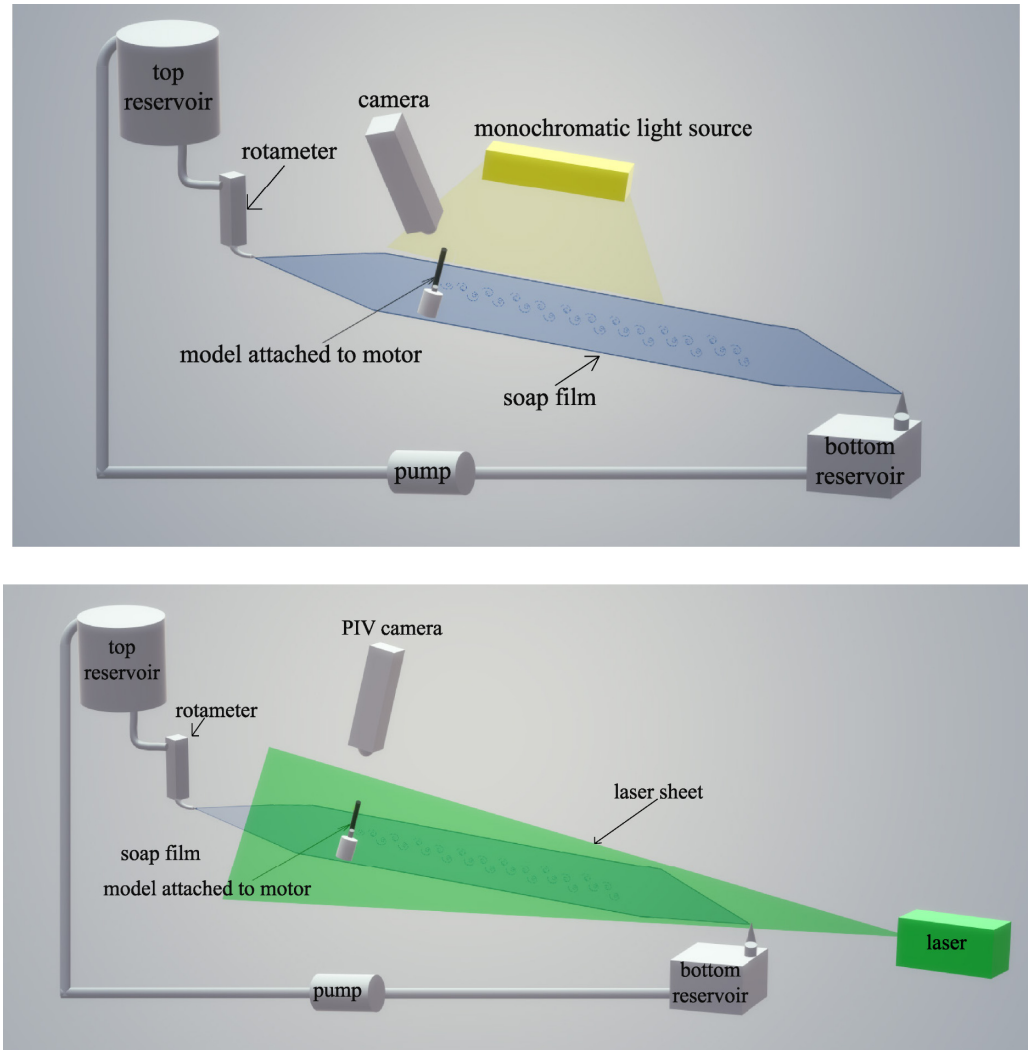

FIG. 4. Schematic of the experimental setup for flow visualization and PIV experiments. (i) Schematic for flow visualization; (ii) schematic for PIV.

transformation of the interference pattern from constructive to destructive and *vice versa*. Flow structures were captured with a DSLR camera (Nikon D810) for still images. A high-speed camera (Dantec Dynamics Motion Pro X3) was used to acquire high frame rate flow visualization data for postprocessing. The camera was mounted on a traverse mechanism, viewing almost right angles to the soap film and capable of traversing parallel to the film. This helps in capturing downstream flow behavior.

C. PIV technique

2D PIV experiments were performed on the soap film tunnel under the same experimental conditions of flow visualization. The soap solution was seeded with 5 μm polyamid seeding particles (from Dantec Inc.), and the film was illuminated using a Nd:YAG dual capacity PIV laser which emits light of 532 nm wavelength from the end of the bottom reservoir [Fig. 4(b)]. A laser

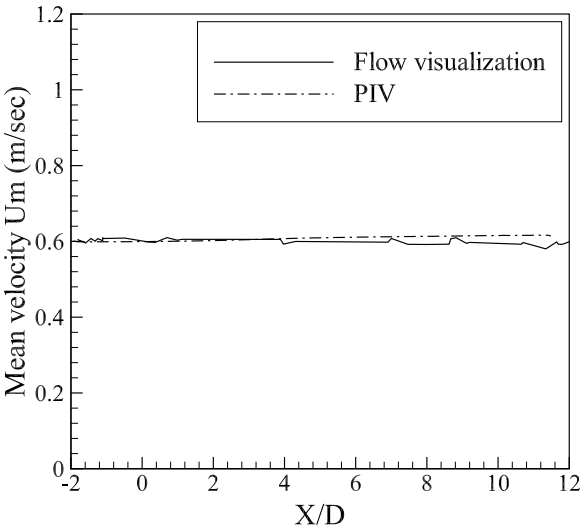

FIG. 5. Mean velocity obtained by flow visualization and PIV technique at 32 ml/min for a $X \sim 12.5D$ long test section.

pulse with a repetition rate of 2.8 Hz, pulse duration of 7 ns, and maximum output energy of 200 mJ per pulse was used in the present experiments. A laser sheet was created by placing a cylindrical lens in front of the PIV laser and focused down to less than 1 mm. The laser sheet was aligned with the soap film as shown in Fig. 4(b), such that the test section gets illuminated. This illuminated seeded flow is captured sequentially using 8 MP CCD TSI camera, which was mounted at right angles to the soap film. A PIV camera with a 100 mm lens was used to capture 30×10 cm^2 of the physical area with a magnification of 4×10^{-3} cm/pixel. The time separation between two frames (or between two laser pulses) was set to 150 μsec.

PIVlab [30] was used to analyze the captured 300 image pairs which were used to obtain averaged PIV data. In the image processing, first a high-pass kernel size was enabled to suppress the low-frequency noise and then FFT window deformation (direct Fourier transform correlation with multiple passes and deforming windows) was used with a 64×64 interrogation window in the first pass and 32×32 interrogation window in the second pass. This results in a high signal-to-noise ratio and good vector resolution.

D. Characterizing the soap film tunnel

This section demonstrates the procedure for the determination of unknowns in the Reynolds number calculation used in the present work.

1. Velocity measurement:

In soap film tunnel experiments, two techniques were used for velocity measurements. An estimate of velocity and its variation was obtained by tracking impurities in soap film using high-speed flow visualization data [31,32]. An accurate measurement of flow field velocity was done using the PIV technique [28]. The procedure for these techniques is stated in Secs. II B and II C. A schematic of the experimental setup for velocity determination is similar to that in Fig. 4, with no object placed in the soap film. Velocity measurements obtained from flow visualization and PIV are shown in Fig. 5 and show that the two techniques give similar results.

Figure 6 shows velocity profiles across the test section at various distances downstream of the cylinder. It shows that velocity is almost uniform with less gradient across the test section in the soap

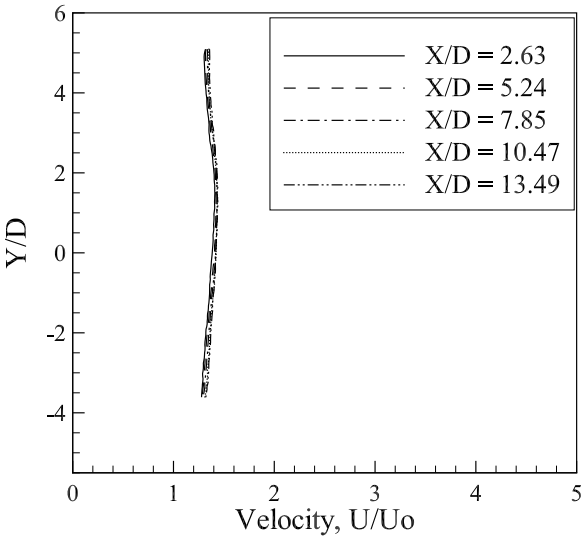

FIG. 6. Normalized velocity profiles at 32 ml/min flow rate at various locations downstream of the flow.

film, suggesting that the rotating cylinder is subjected to uniform flow. The considerable length of the soap tunnel helped in the study of downstream wake morphology. As the tunnel is tilted, a gentle velocity gradient exists in the downstream direction due to the gravity component, but air drag gives a countereffect reducing its magnitude to a smaller extent. Table I shows the variation of velocities at various distances downstream of the cylinder.

The mean velocity across the test section at the cylinder streamwise location (Fig. 2) was considered as free-stream velocity (U_o). Free-stream velocity at flow rates of 24 ml/min and 32 ml/min was obtained as 0.534 m/sec and 0.630 m/sec, respectively, resulting in a Reynolds number of 200 and 250 for the cylinder used.

2. Fluid properties

Density (ρ) of the soap solution is measured directly using an accurate weighing machine and was obtained as 974.8 kg/m^3. Dynamic viscosity was determined indirectly by the method suggested by Gharib and Derango [25], which uses Roshko's empirical relation between St and Re to determine the dynamic viscosity. From the obtained dynamic viscosity, the St versus Re curve was plotted and was justified because the dynamics in soap films are 2D counterparts of their 3D vortex shedding process. Using this method, dynamic viscosity (μ) was calculated as obtained as 242×10^{-4} Pa·s in the present experiments. From the obtained dynamic viscosity and density, kinematic viscosity (ν) was calculated as 24.8×10^{-6} m^2/sec. With the known properties and velocity field of the soap film test section, a Reynolds number at various flow rates was calculated. These property values were used to ascertain the onset of vortex shedding in a circular cylinder. Figure 7 shows that at Re $\sim$42 the vortex shedding activity begins, which is in agreement with the published literature on flow past circular cylinders. Figure 7 also shows the wake just before

TABLE I. Mean velocity variation at various distances measured using flow visualization.

Streamwise distance(X)	0*D*–16*D*	17*D*–33*D*	34*D*–50*D*	51*D*–67*D*	68*D*–85*D*
Mean velocity (m/sec)	0.60	0.65	0.72	0.75	0.77
Error percentage (%)	1.19	0.96	2.93	1.38	1.68

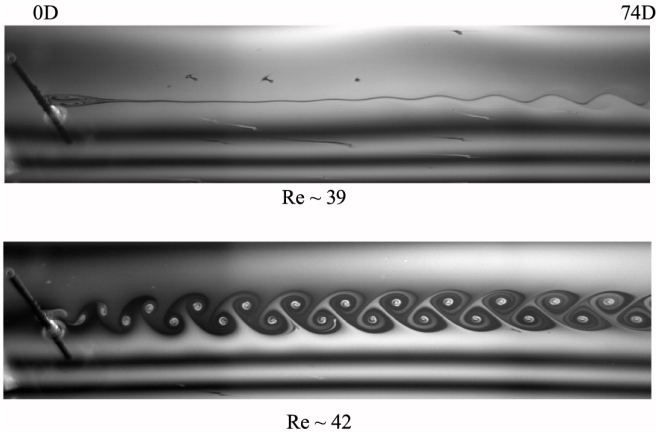

FIG. 7. Initiation of von Kármán vortex shedding at Re ∼ 42.

vortex shedding begins at Re ∼39 where two attached eddies and an undulating wake are clearly visible. This validates the setup of the present soap film tunnel. In the present experimental study of rotating cylinders in the soap film tunnel, wake morphology for various cylinders both hydrophobic and nonhydrophobic is observed for a rotation rate ranging from 0 to 4.36 at Re ∼ 200 and 250.

III. RESULTS AND DISCUSSION

Flow visualization data of nonhydrophobic rotating cylinder at Re ∼ 250 are presented in Fig. 8 for different rotation rates. The imaged area is about $28D$ in streamwise extent. Flow visualization at $\alpha = 0$ shows the classic von Kármán vortex street shed from the cylinder. As the rotation rate increases from $\alpha = 0$ to 2.26, a distinct Kármán vortex shedding is observed with few extra vortices in between. From $\alpha = 0$ to 2.26, the increase in rotation rate decreases the speed of the flow at the top relative to the bottom surface of the cylinder. This provides high momentum to small attached counterclockwise vortices generated at the bottom surface, making it shed rather than to coalesce as a single big vortex. Figure 9 shows the variation of the ratio of the counterclockwise vortex shedding frequency to clockwise vortex shedding frequency with the rotation rate at Re ∼ 200 and 250. The ratio of the number of shed counterclockwise vortices to clockwise vortices is one at $\alpha = 0$, whereas its value increases with more number of shed counterclockwise extra vortices at $\alpha = 1.2$, for 3 sec of flow visualization data at Re ∼ 250. The reason for the peak is nona-malgamation of small vortices in the high momentum region. This weakens the strength of shed counterclockwise vortices (Fig. 13 below) relative to the shed clockwise vortices in addition to the wrapping of counterclockwise vorticity around the cylinder. Subsequently, the number of shed counterclockwise vortices decreases, and the ratio falls below unity at $\alpha = 1.8$.

At Re ∼ 200, a similar trend is seen with a maximum ratio of 2.48 at around $\alpha = 2.17$. It can be inferred that relatively more shed counterclockwise vortices are seen before the commencement of the transition zone.

The regime of transition from von Kármán to single-sided vortex shedding appeared near $\alpha =$ 2.56 to 2.93 and is termed the transition zone. The suppression of vortex shedding is not observed in the present experiments in the soap film unlike as stated in recent experimental and numerical studies on rotating the cylinder [10,11]. In the regime of $\alpha = 2.93$ to 4.36, the vortex street remains as single-sided in a clockwise sense with different rates of the detachment of eddies. The flow is observed to be unsteady throughout the entire range of rotation rates. The rotation of the cylinder results in the motion of the separation points over the cylinder, which in turn results in the deflection of the vortex street in the direction of rotation. The deflection of vortex shedding is evident in Fig. 8 from $\alpha = 0$ to 4.36.

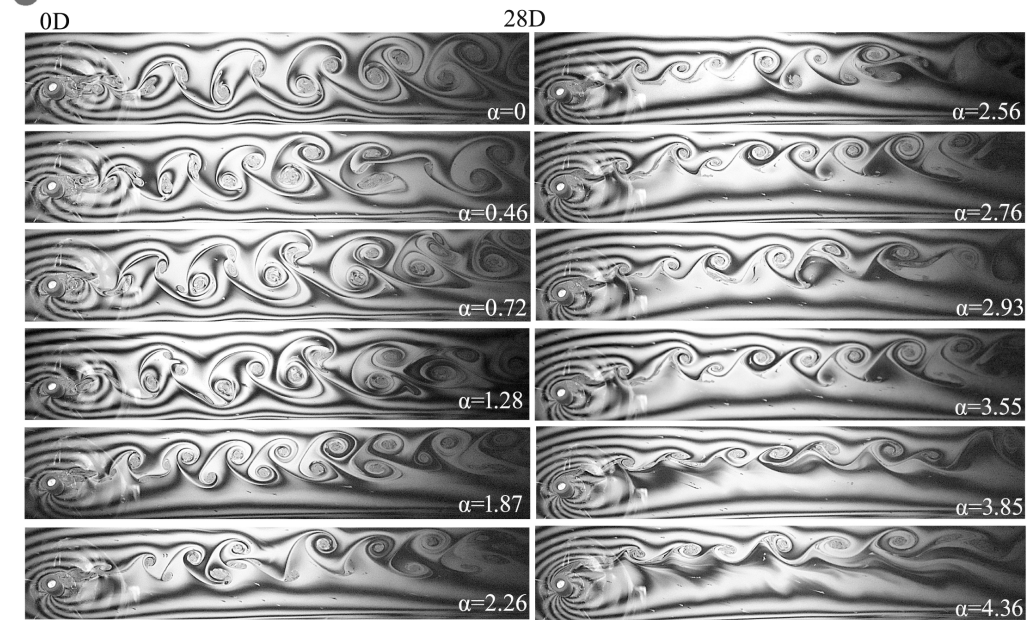

FIG. 8. Wake structures of the nonhydrophobic rotating cylinder at various counterclockwise rotation rates at Re $\sim$ 250.

Vorticity maps of the wake structure were obtained using PIV measurements to get quantitative information of the wake structure seen in the flow visualization with particular emphasis on single-sided vortex shedding. Figure 10 shows a normalized vorticity field variation for the nonhydrophobic cylinder at various α from 0 to 4.36 at Re $\sim$ 250, having flood line spacing -13 to

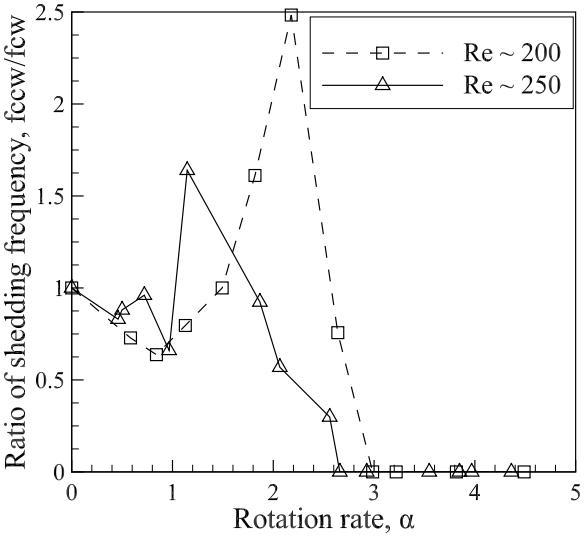

FIG. 9. Variation in the ratio of shedding frequency of counterclockwise to clockwise vortices with rotation rate, α.

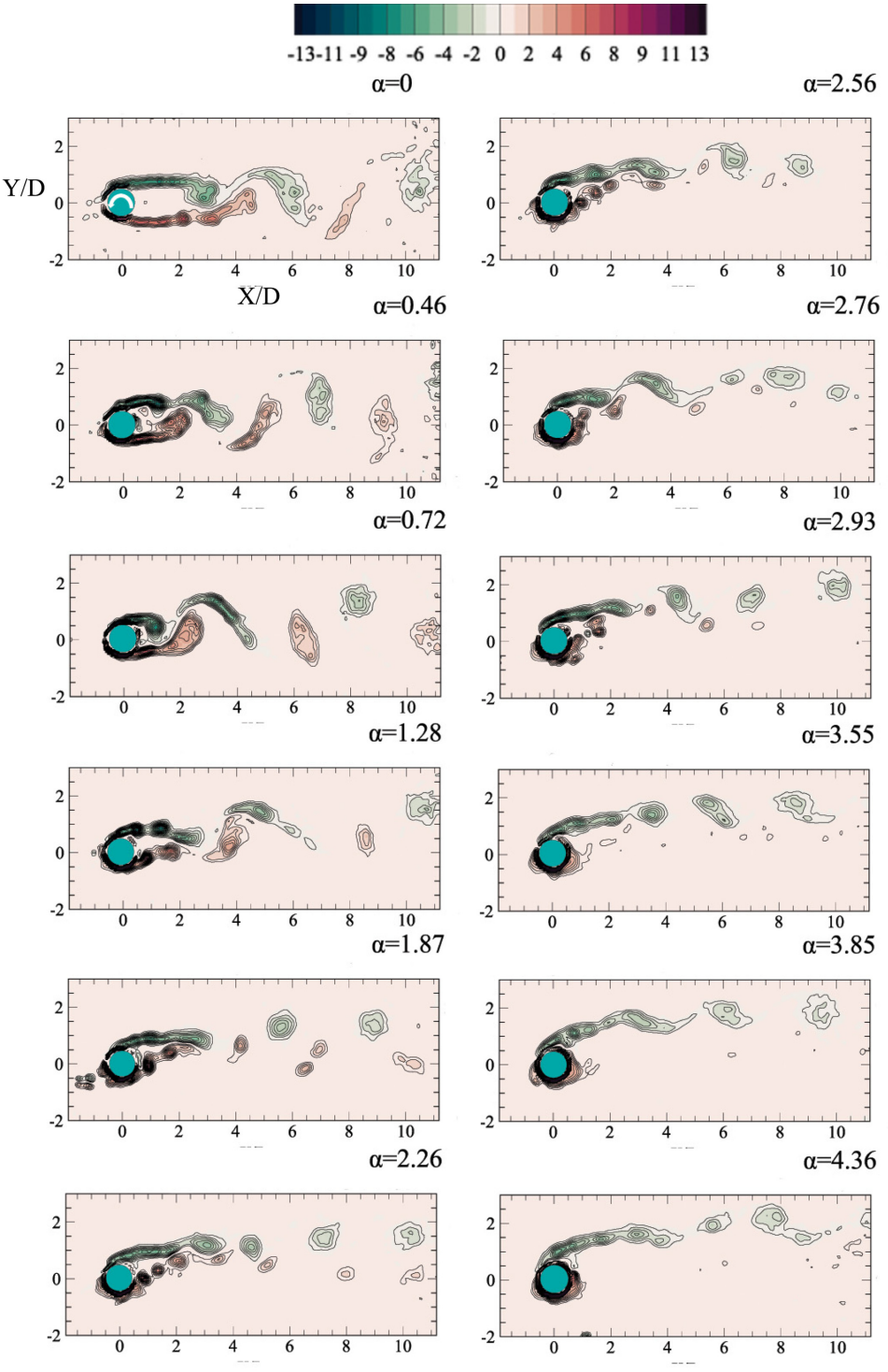

FIG. 10. Instantaneous vorticity field (ω D$/U_o$) variation of nonhydrophobic rotating cylinder at various rotation rates at Re $\sim$ 250. The cylinder is rotating counterclockwise.

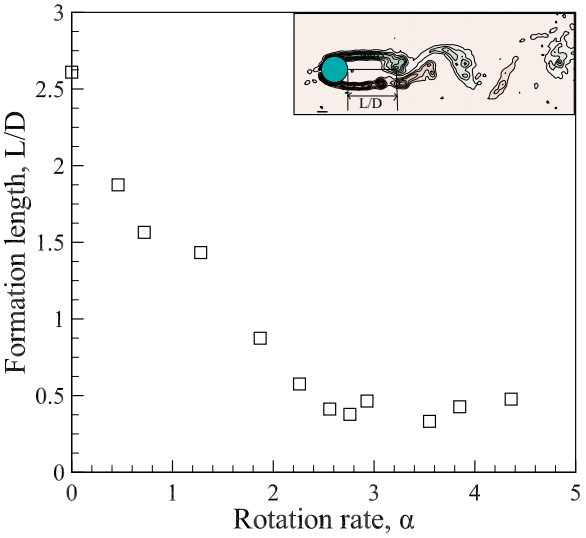

FIG. 11. Formation length variation with rotation rate using PIV experimentation.

13 with a step size of 0.79. The vorticity maps clearly show the alternating shedding of vortices and the deflection of vortex street in the direction of rotation from $\alpha = 0$ to 2.26, whereas from $\alpha = 2.56$ to 2.93, counterclockwise vortices of weak strength (vorticity patches) are shed from the bottom part of the cylinder (Fig. 10). Hence this regime is considered to be a transition zone from von Kármán vortex shedding to single-sided vortex shedding. Eventually, as the rotation rate increases to 4.36, counterclockwise vorticity gets wrapped around the cylinder, with no vortices of counterclockwise sign being shed. The vorticity field variation clearly shows the wake region behind the cylinder at various rotation rates.

The length of the recirculation region of the wake behind the cylinder indicates the amount of slow-moving fluid. The recirculation region is enclosed by the two shear layers peeling off the two sides of the cylinder and touching each other on the average. Vortex shedding occurs only if vorticity of enough strength is accumulated in the region of slow-moving fluid, preferably recirculating fluid [10]. Figure 11 shows the variation of the formation length, L/D, with α. The inset of the figure shows the formation length schematic. The drastic reduction in formation length from $\alpha = 0$ to 2.76 is seen in Fig. 11.

As the amount of slow-moving fluid decreases, the strength of vortices shed from the surface of the cylinder also decreases. This variation of the strength of the first shed vortices from the surface of the cylinder is shown in Fig. 12. Using PIV, circulation of vortices shed from the surface of the cylinder was determined, and the strength of vortices is expressed in terms of its normalized circulation value, Γ/U_oD. At $\alpha = 0$, the strength of both counterclockwise and clockwise vortices shed is 2.62 and 2.82, respectively. The increase in the strength of both counterclockwise and clockwise shed vortices to 2.97 and 3.12, respectively, is observed as the rotation rate increases to 0.72. At this α, both clockwise and counterclockwise shed vortices have maximum strength. Subsequently, the increase in rotation rate causes a decrease in the strength of shed counterclockwise vortices to a minimum value of 0.38 at $\alpha = 2.93$, which eventually disappears, whereas the strength of shed clockwise vortices initially decreases to 1.6 at $\alpha = 2.26$ and subsequently does not show any definite trend. Figure 12 also shows that the clockwise vortices are always stronger than the counterclockwise vortices shed from the cylinder.

To understand the relative strength of the shed vortices, the ratio of clockwise to counterclockwise circulation of the first shed vortex is plotted in Fig. 13. It shows that as the rotation rate increases, the ratio initially remains almost constant and then increases showing the increase in

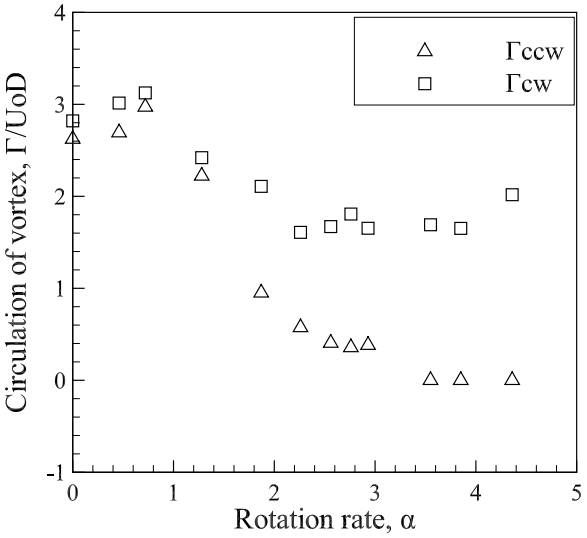

FIG. 12. Variation of the normalized circulation of vortices shed from the cylinder with rotation rate, α.

the relative strength of clockwise vortex. The circulation ratio, in the range of $\alpha = 0$ to 1.28, is almost unity, demonstrating that counterclockwise and clockwise vortices shed from the cylinder are of almost equal strength. At $\alpha = 1.87$, the strength of the clockwise vortex becomes twice that of the counterclockwise. Subsequently, as the rotation rate increases the circulation ratio reaches a maximum of 4.5 at $\alpha = 2.76$. At a higher rotation rate above the transition zone, counterclockwise vortices are not shed. It can be inferred from Fig. 13 that, in the region of transition, the relative strength of the shed clockwise vortex reaches a maximum.

To understand the vorticity distribution and its dynamics around the cylinder, the mean vorticity field (averaged over 300 frames) was determined using PIV data. Figure 14 shows the mean vorticity field variation with rotation rate, α, around the cylinder. At $\alpha = 0$, both counterclockwise and

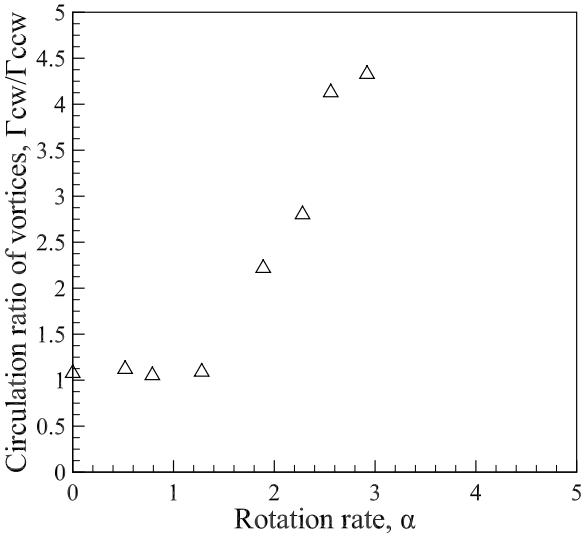

FIG. 13. Variation of ratio of circulation (Γ_{cw}/Γ_{ccw}) of vortices shed from the cylinder with rotation rate, α.

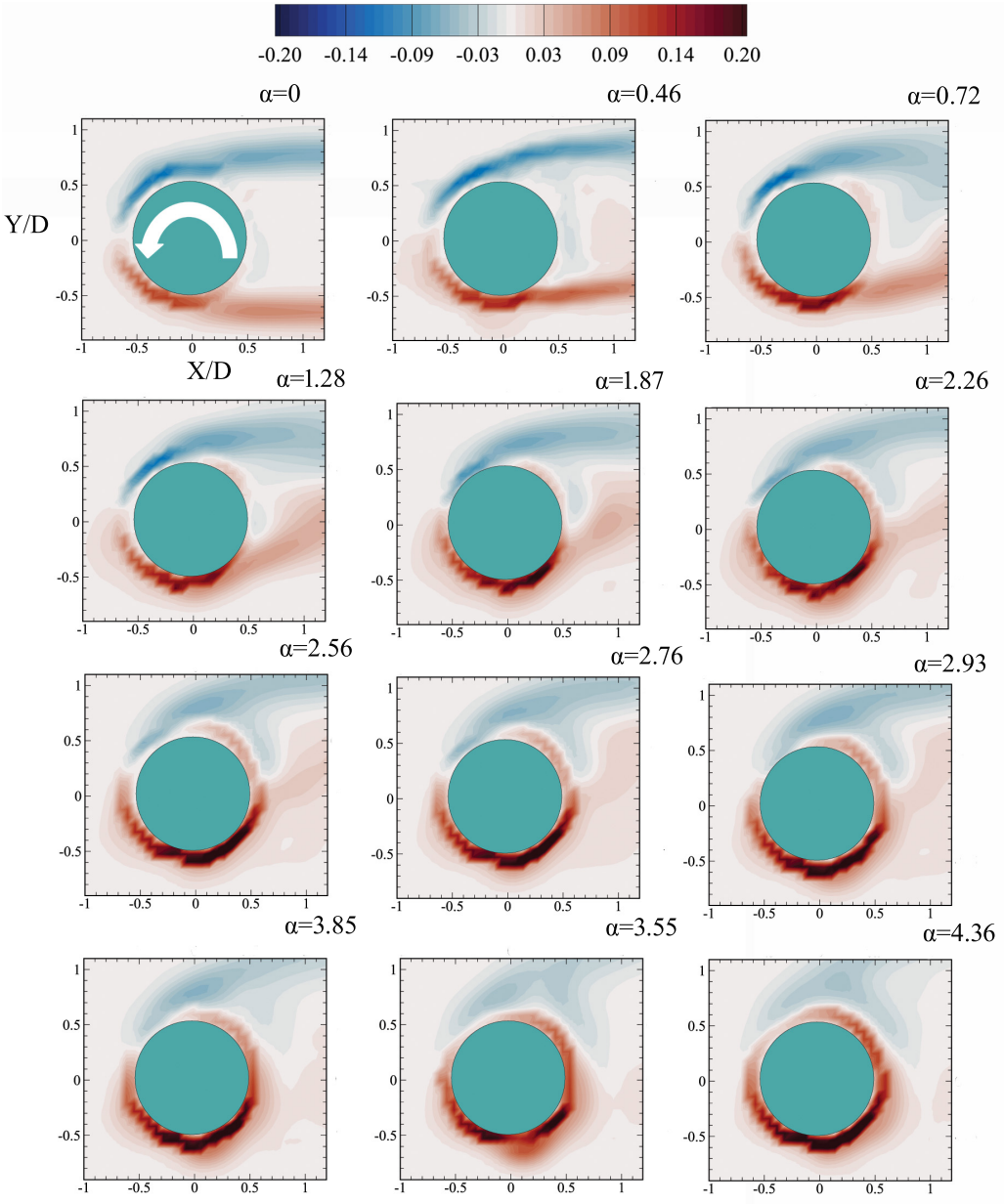

FIG. 14. Mean vorticity field (ω D/U_o) variation over a nonhydrophobic rotating cylinder with rotation rate, α at Re $\sim$ 250.

clockwise vorticity layers form around the cylinder, which develop in the wake region and shed as vortices with the fluid flow downstream. As the rotation rate increases, both the clockwise and counterclockwise vorticity generated over the cylinder gets deflected upwards, as observed until $\alpha = 1.87$. At $\alpha = 2.26$, counterclockwise vorticity almost wraps three quarter of the cylinder surface, whereas clockwise vorticity remains deflected upwards. The increase in the thickness of closed streamlines with rotation rates made the counterclockwise vorticity wrap entirely around the cylinder as seen at $\alpha = 4.36$.

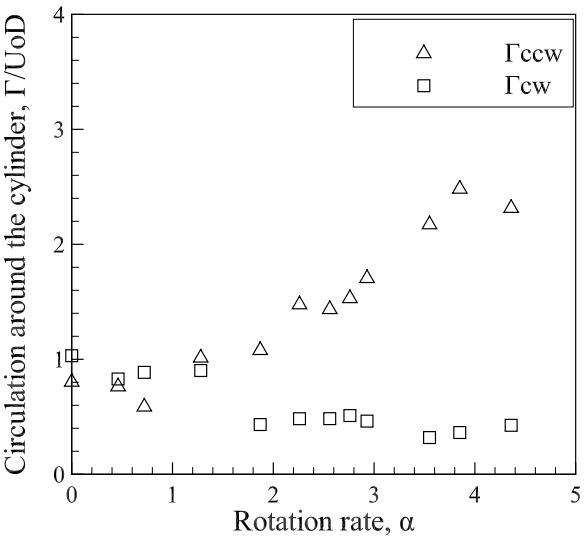

FIG. 15. Variation of the mean normalized circulation around the cylinder with rotation rate, α.

Circulation around the cylinder was obtained by area integrating the mean vorticity field shown in Fig. 14. Figure 15 shows the mean normalized circulation, Γ/U_oD variation of the counterclockwise and clockwise vorticity generated over the cylinder with rotation rate. At $\alpha = 0$, the clockwise and counterclockwise circulation is 1.03 and 0.8, respectively. This slight difference could possibly be due to slight variation in flow velocity on two sides of the cylinder surface. Rotation of the cylinder weakens the clockwise circulation generated at its top surface to a value of 0.25 at $\alpha = 4.36$, whereas the circulation associated with counterclockwise vorticity strengthens up to a value of 2.5 at $\alpha = 3.85$ and again decreases to 2.32 at $\alpha = 4.36$. The relative strength of the counterclockwise to clockwise mean circulation magnitude generated around the cylinder is shown in Fig. 16. It can

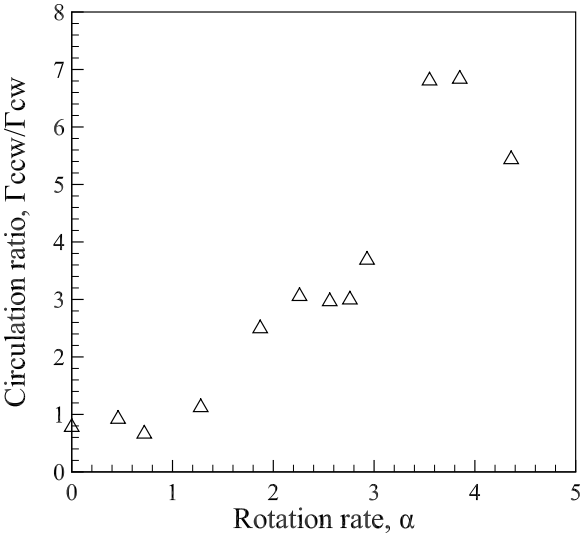

FIG. 16. Variation of ratio of mean circulation, Γ_{cw}/Γ_{ccw} of around the surface of the cylinder with rotation rate, α.

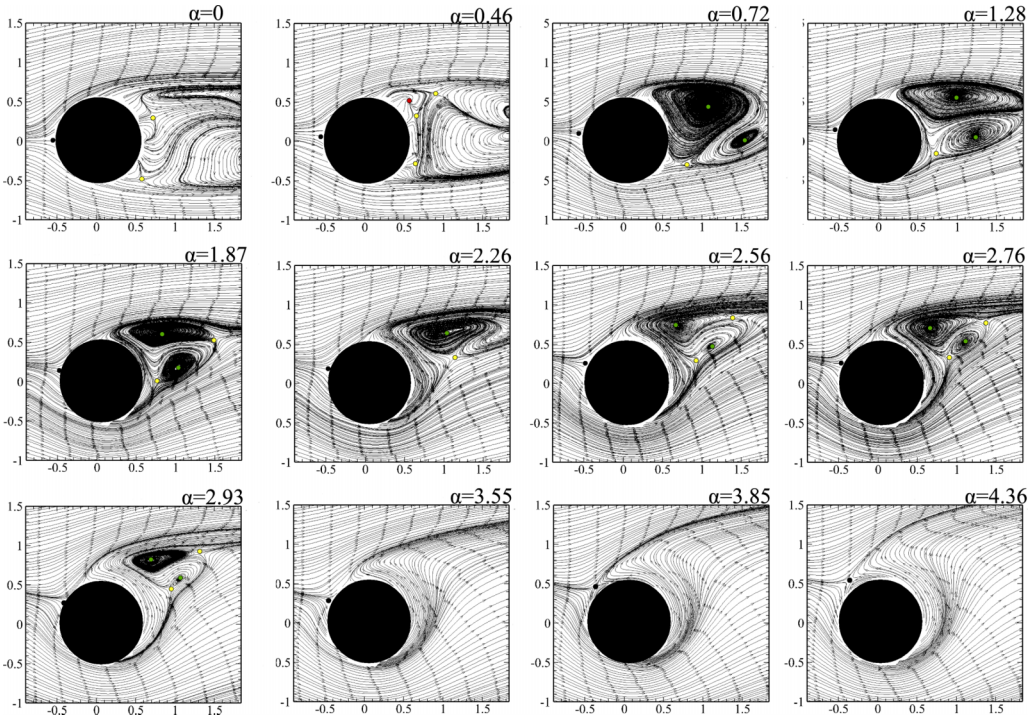

FIG. 17. Mean streamline flow over nonhydrophobic rotating cylinder with rotation rate, α, at Re $\sim$ 250. Front stagnation point, saddle point, node, and vortex center are represented by black, yellow, red, and green dots, respectively. The lifted-off stagnation point for $\alpha = 3.85$ and 4.36 is shown with a black dot.

be seen that until $\alpha = 1.28$, the ratio remains almost unity. At $\alpha = 1.87$, the ratio exceeds 2, and as the rotation rate increases, it reaches a maximum value of $\sim$7 at $\alpha = 3.85$. It is observed that the ratio decreases to a value of 5.5 at $\alpha = 4.36$, which may happen due to the enhanced diffusion of counterclockwise vorticity resulting from sharp gradients in closed streamlines surrounding the cylinder.

Ren *et al.* [20] from his observations stated that as the rotation rate increases, circulation around the cylinder increases, which changes the location of stagnation point correspondingly. To get insight into the near-wake flow topology and understand the effect of circulation on the location of stagnation point, the streamline pattern near and around the cylinder was examined for the averaged flow field. Figure 17 shows the averaged streamline flow field around the cylinder at Re $\sim$ 250. Figure 17 shows that the motion of the front stagnation point is in an opposite direction to the sense of cylinder rotation, whereas the rear stagnation point moves in the same direction as the rotation of the cylinder. At a rotation rate of around 3.85, both the front and rear stagnation points join and get lifted off from the surface of the cylinder creating a saddle point and a boundary of closed streamlines around the cylinder. This happens due to fully wrapped counterclockwise circulation around the cylinder as shown in Fig. 14. The distance of the saddle point from the center of the cylinder increases with the increase in the rotation rate, which shows an increase in the thickness of closed streamline layer. The thickness of the closed streamline layer can be associated with the strength of counterclockwise circulation wrapped around the cylinder. The location of the front stagnation point with an increase in rotation rate for an averaged [averaged over 300 frames, which translates to number of cylinder rotations varying from 0 to 31 (approx.) for α ranging from 0 to 4.36 for Re $\sim$ 250, respectively] flow is shown in Fig. 18 in terms of its angle (in degrees) with the horizontal along the flow direction. It can be seen from the location of lifted-off stagnation point at

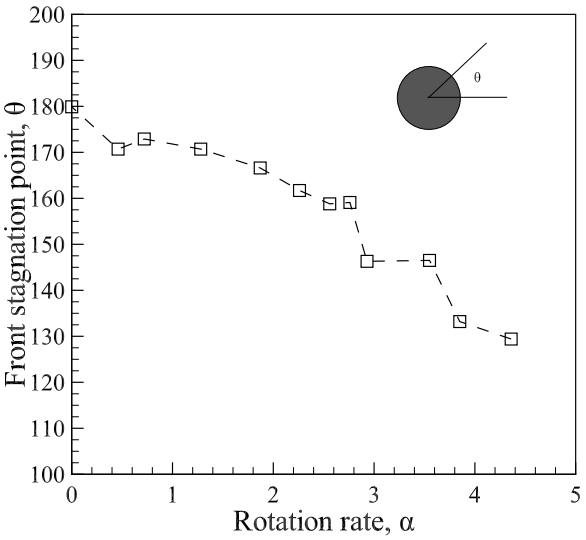

FIG. 18. Motion of front stagnation point (averaged data) in degrees with rotation rate, α.

$\alpha = 3.85$ in Fig. 18 that it is slightly situated towards the upstream side for an averaged flow rather than symmetrically above as in the case of potential flow description. This suggests that the motion of the front and rear stagnation points is asymmetrical unlike the situation shown in the potential flow case in textbooks.

The possible reason for the no suppression results obtained in soap film tunnel experimentation is perhaps the asymmetric motion of the stagnation points. From the results shown in Fig. 17 at $\alpha = 3.85$, front and rear stagnation points get merged and lifted off from the surface at $\sim 135^\circ$, whereas the numerical investigation of Mittal and Kumar [10] shows that its location is $\sim 90^\circ$ at $\alpha = 4$. The reason behind it could be dissimilarity in the motion of the front and rear stagnation point, which made them merge at $\sim 135^\circ$. At the transition regime, attached vortices of the same sign as that of the rotation of the cylinder are created inside the boundary layer at the bottom surface of the cylinder, unlike as stated in Mittal and Kumar [10]. These can be transported either by diffusion or by advection or both. But a thick layer of fluid around the cylinder does not help in advection, so the sole transportation is by diffusion. Mittal and Kumar suggested that counterclockwise vorticity of significant strength is fed to the stagnation point, where vorticity accumulates with time and gets shed. However, in the present experiments, as the rotation rate increases, counterclockwise vorticity gets wrapped around the cylinder without being fed to the stagnation point due to its location on the windward direction, and its movement towards the stagnation point is hindered by the clockwise vorticity at the top of the stagnation point. So these attached counterclockwise vortices, having weak strength, do not get diffused out of the thick layer of fluid due to their location below the stagnation point, whereas clockwise vorticity is advected downstream creating single-sided vortex shedding having vortices of the opposite sign of rotation as that of the rotating cylinder. It appears that the motion of the stagnation point plays a dominant role in the wake morphology, which in turn depends upon the distribution of counterclockwise and clockwise vorticity around the cylinder.

Another interesting feature observed from the mean streamline flow field in Fig. 17 is the generation and annihilation of critical points downstream of the cylinder, with the increase in rotation rate. In Fig. 17 the critical points near the cylinder are shown with different colored points. The following section gives an outlook about the critical points formed near the surface of the cylinder at various rotation rates. Initially, at $\alpha = 0$, two saddle points are seen just behind the cylinder, with two vortex centers a little ahead in the wake region. A node is created near the top saddle point at $\alpha = 0.46$ near the cylinder. This annihilates the near saddle point moving the vortex

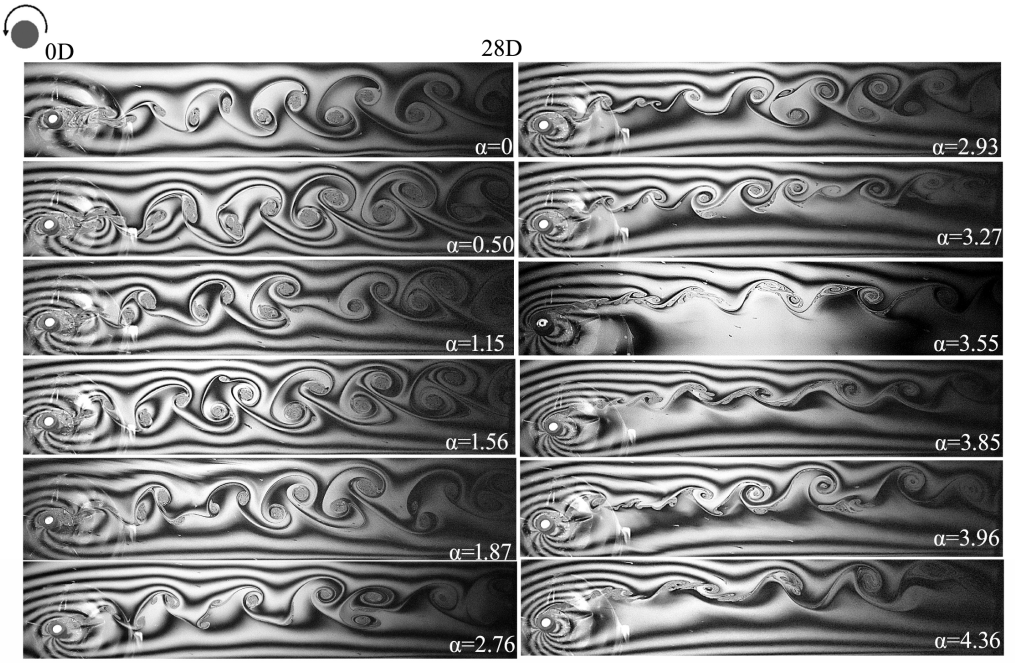

FIG. 19. Wake structures of hydrophobic cylinder of level I at various counterclockwise rotation rates for Re $\sim$ 250.

centers upstream of the flow at $\alpha = 0.72$ as α is increased. It is evident that the distance between the saddle point and the vortex center gets decreased as the rotation rate increases to 1.87. At $\alpha = 2.26$, the annihilation of the bottom vortex with the saddle point is seen. In this way, saddle points demolish the vortex centers in the wake region, making it disappear as seen at $\alpha = 3.55$. Consequently, at higher rotation rates (i.e., $\alpha = 3.85$ and 4.36), no recirculation region of the wake is seen. The mean deflection of the recirculation region in the wake can be known from the streamline flow field. With an increase in rotation rate from 0 to 2.26, the deflection of the wake is observed to be $\sim$22.8°. At the transition zone, the wake shows a deflection of $\sim$35° to 40°. Subsequently, no recirculating region is seen with the flow deflection to $\sim$35° to 40° near the top stagnation point.

A. Effect of hydrophobicity and Reynolds number

Special behavior of hydrophobic cylinders in a flow field like a delay in the Reynolds number at which vortex shedding starts and an increase in the length of recirculation region in wake as stated in Muralidhar *et al.* [17] has motivated the present study on hydrophobic surfaces to observe its effect over wake structure of a rotating cylinder both qualitatively and quantitatively. Figure 19 to 21 show the flow visualization data of the wake structure of a rotating cylinder having various hydrophobicity levels at Re $\sim$ 250. The main interest in the study of hydrophobic surfaces is to see the single-sided vortex shedding and understand the effect on its onset. Wake deflection is evident in all three hydrophobic surfaces in the α range 0 to 4.36. No evidence of suppression is seen in all the hydrophobic cylinders as in the nonhydrophobic cylinder case. Figure 19 shows the wake morphology of the rotating cylinder of hydrophobicity level I. For this cylinder, as the rotation rate increases to 2.93, distinct von Kármán vortex shedding is observed due to dissimilarity in the peripheral velocities at top and bottom surfaces. However, due to cylinder rotation the two vortices of the shed vortex pair have different strengths, and in addition few extra vortices are seen. A similar

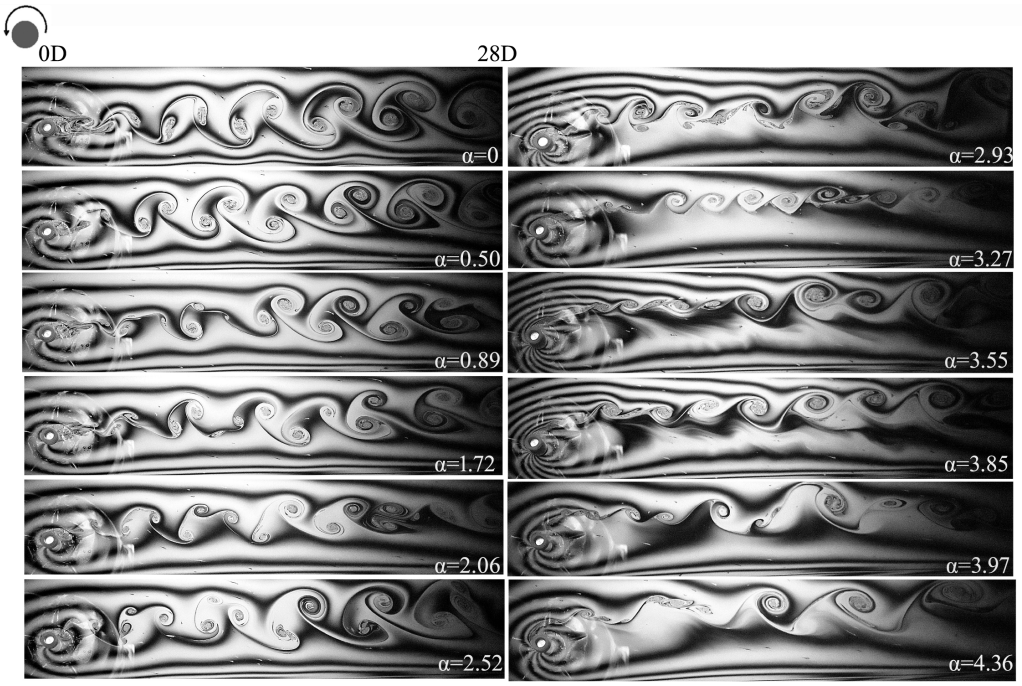

FIG. 20. Wake structures of hydrophobic cylinder of level II at various counterclockwise rotation rates at Re $\sim$ 250.

kind of vortex shedding is observed until 2.93 in the cases having hydrophobicity levels II and III (Figs. 20 and 21).

Figure 22(a) showing the relative number of shed counterclockwise to clockwise vortices at Re $\sim$ 200 for nonhydrophobic and hydrophobic cylinders shows that for a hydrophobic cylinder of level I, f_{ccw}/f_{cw} increases to 1.2 with rotation rate until around $\alpha = 2.3$ and then it decreases until the transition zone for Re $\sim$ 200 whereas the trend remains almost the same until $\alpha = 2.4$ for Re $\sim$ 250 [Fig. 22(b)]. Hydrophobic cylinders of level II and III have a maximum ratio of 1.5 for counterclockwise to clockwise vortices shed per second at $\alpha = 2.5$ at Re $\sim$ 250. Correspondingly, for Re $\sim$ 200 the ratio reaches a maximum of 1.26 and 2.5 at $\alpha = 2.4$ and 2 for cylinders of hydrophobicity levels II and III, respectively. Although no definite trend is observed for variation of the ratio of shedding frequency, f_{ccw}/f_{cw}, it can be inferred that relatively more counterclockwise vortices are shed before the commencement of the transition zone for all the cylinders. In addition, the peak value of the shedding frequency ratio increases with the strength of hydrophobic surfaces. It can be noted that hydrophobic surfaces behave differently from nonhydrophobic surfaces, in particular, on the onset of the transition zone. As the surface becomes hydrophobic, the rotation rate at which the transition zone occurs increases. This shows that the strength of hydrophobicity has an effect on the onset of the transition zone at Re $\sim$ 250. This fact can be supported by the dependence of the new vortex shedding mode on the strong shear layer near the upper side of the cylinder as suggested by Ren *et al.* [20].

For a hydrophobic surface, to remedy the loss of shear effect, a higher rotation rate is required for the initiation of the new mode of vortex shedding, which increases the rotation rate at the onset of the transition zone for hydrophobic cylinders. The regime of transition is observed from $\alpha =$ 2.93 to 3.27 for hydrophobic cylinder of levels I and II, whereas it is from $\alpha = 2.93$ to 3.12 for a hydrophobic cylinder of level III. Consequently, the wake structure remains single-sided with clockwise vortices until $\alpha = 4.36$ for all the hydrophobic cylinders.

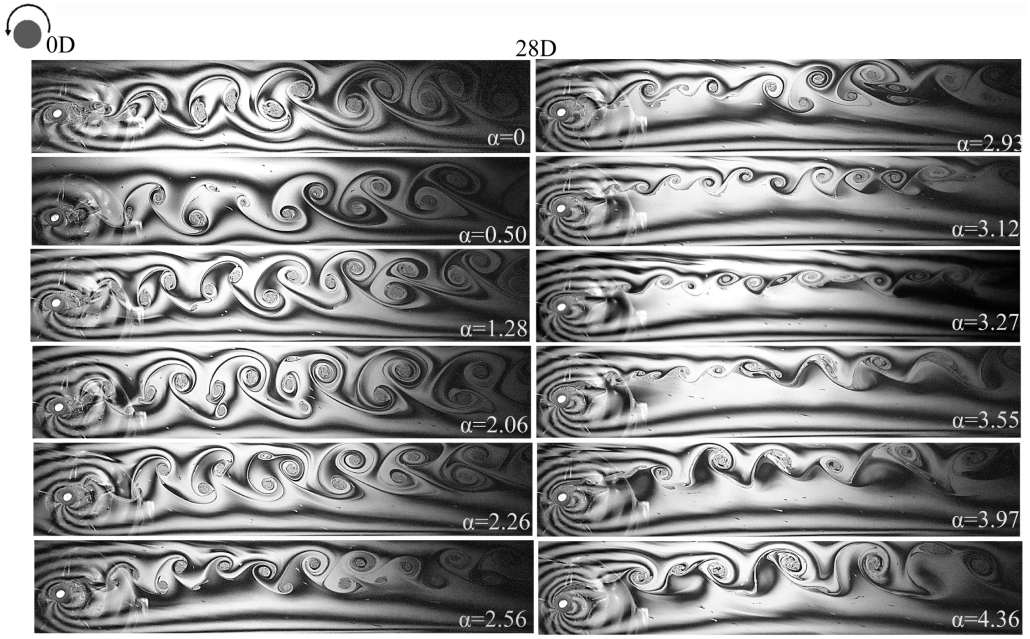

FIG. 21. Wake structures of hydrophobic cylinder of level III at various counterclockwise rotation rates at Re $\sim$ 250.

Figure 23 shows the wake morphology in the transition zone for both nonhydrophobic and hydrophobic cylinders at Reynolds numbers of 200 and 250. For a nonhydrophobic rotating cylinder, as the Reynolds number decreases from 250 to 200, the rotation rate for the onset of transition increases from 2.56 to 2.64. A similar kind of behavior is observed for other hydrophobic cylinders (shown in Fig. 23). It can be stated that a hydrophobic rotating cylinder at a particular Re value

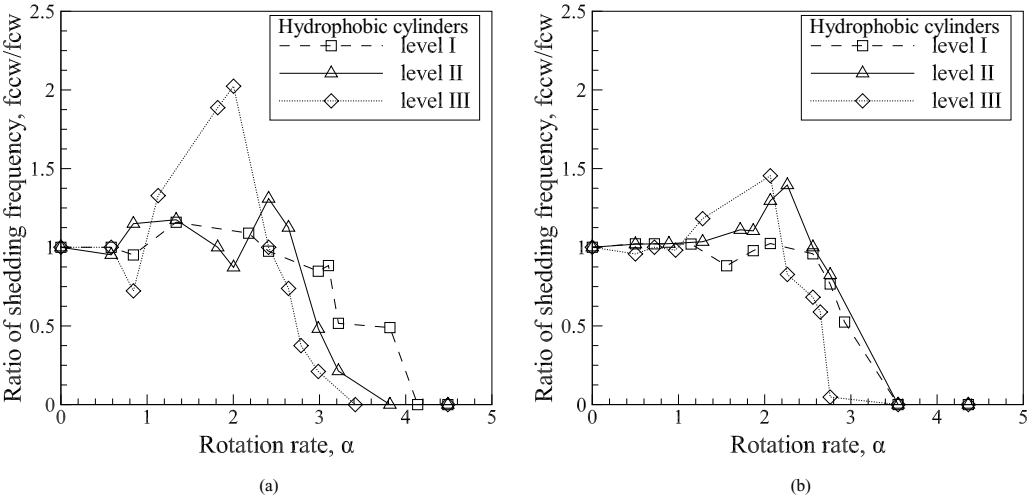

FIG. 22. Variation in ratio of shedding frequency of counterclockwise vortices to clockwise vortices for nonhydrophobic/hydrophobic cylinder of levels I, II, and III with rotation rate, α at (a) Re $\sim$ 200 and (b) Re $\sim$ 250, respectively.

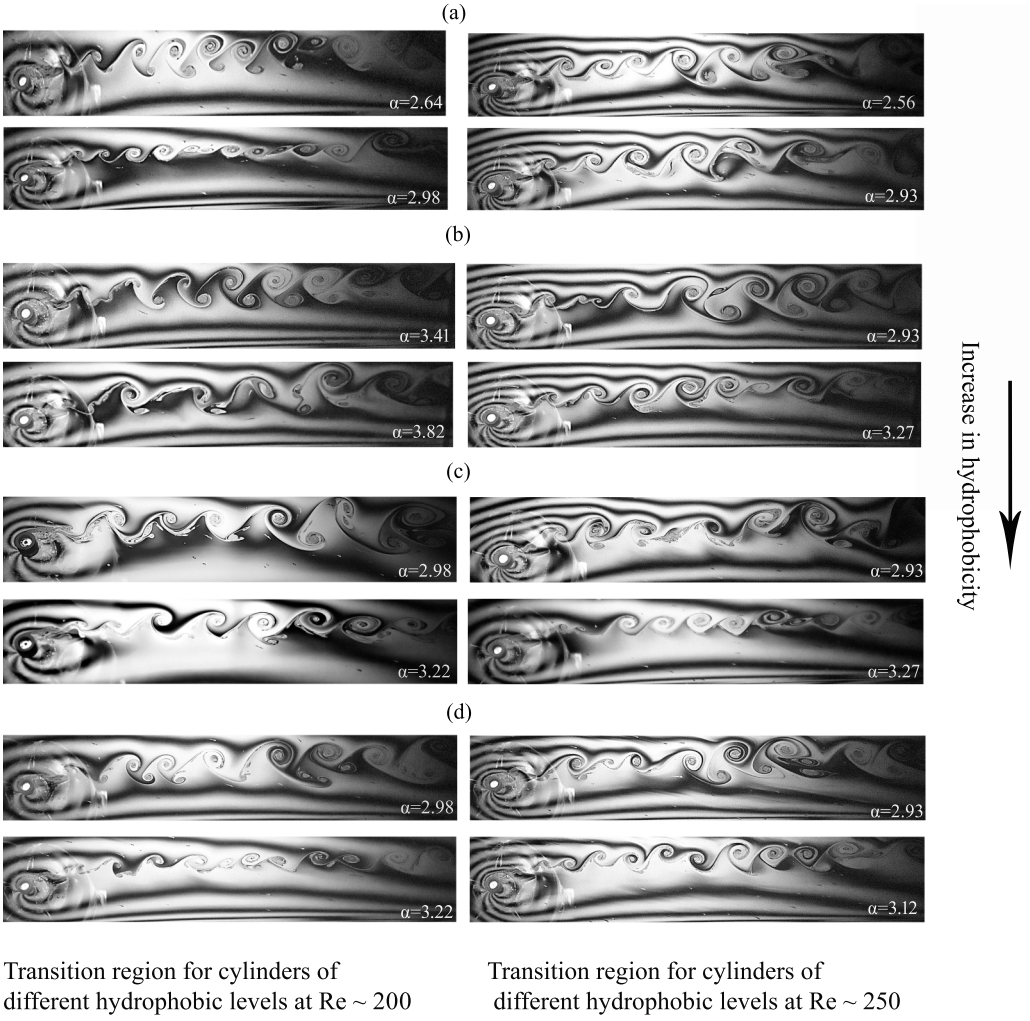

FIG. 23. Effect of Reynolds number and hydrophobicity over the onset of transition zone. (a) Nonhydrophobic cylinder, (b) hydrophobic cylinder of level I, (c) hydrophobic cylinder of level II, and (d) hydrophobic cylinder of level III.

behaves as if a nonhydrophobic rotating cylinder placed at low Reynolds number flow conditions. The reason is perhaps related to the less shear generated (vorticity generated) over the surface in hydrophobic surfaces, which is comparable to the nonhydrophobic surface cylinder at low Reynolds number flow conditions. The magnitude of interval of transition zone remains almost the same for all the cylinders irrespective of the flow conditions (i.e., Reynolds number) and hydrophobicity.

A rotating cylinder has a potential application of wake structure modification, which may reduce vortex-induced vibrations where vortex shedding frequency (Strouhal number) plays an important role. In determining the Strouhal number, the frequency of the shed vortices, f_s, was obtained by counting the clockwise vortices at a streamwise distance of $X \sim 14D$ for 3 sec. The study gave a Strouhal number value of 0.197 at Re $\sim$ 200, which is in excellent agreement with the published literature value [10,33]. In general, the Strouhal number increases as the rotation rate increases until the transition region and then it gradually decreases. The Strouhal number

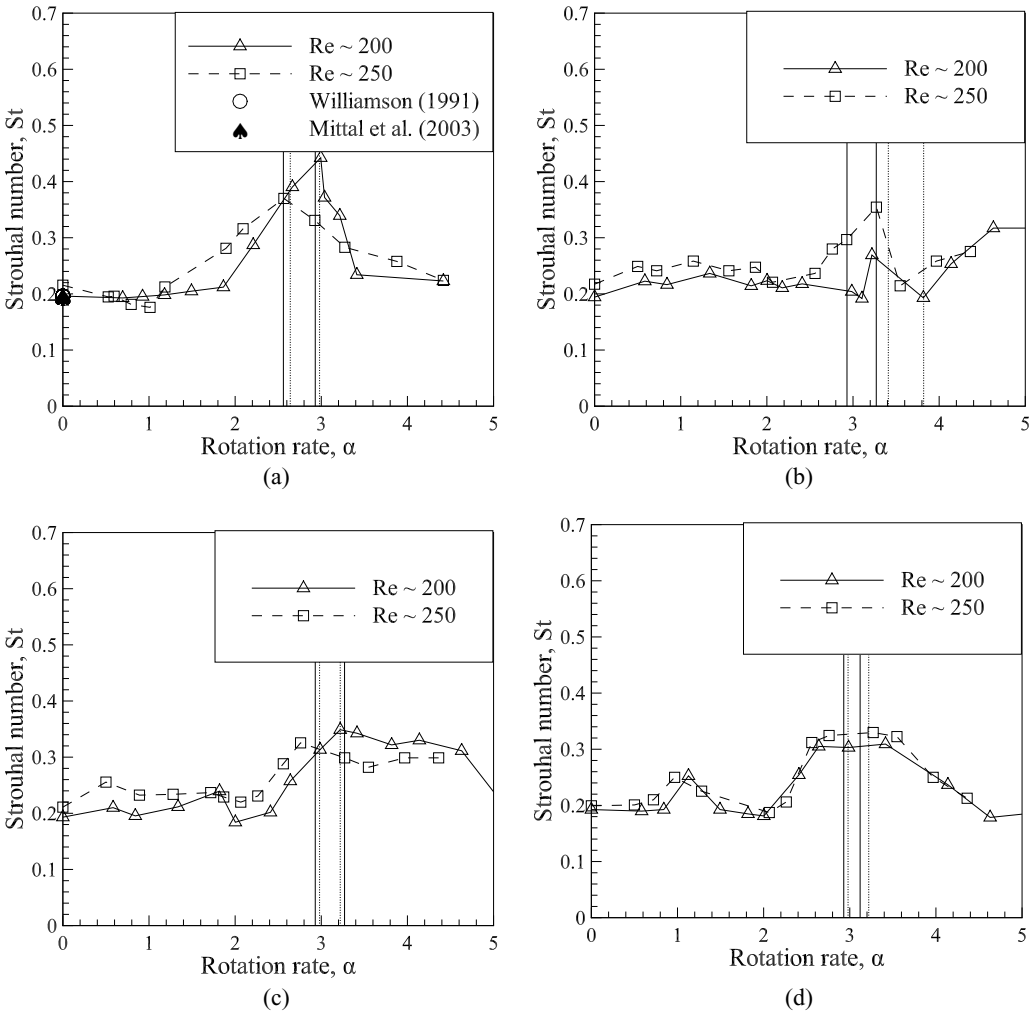

FIG. 24. Strouhal number variation for (a) non-hydrophobic cylinder, (b) hydrophobic cylinder of level I, (c) hydrophobic cylinder of level II, (d) hydrophobic cylinder of level III, with rotation rate at Re $\sim$ 200 and 250, and transition region is shown for Re $\sim$ 200 and 250 as dotted and solid vertical lines, respectively.

variation in the range before the commencement of the transition zone shows some uncertainties. In spite of the uncertainties stated above, it can be concluded that the maximum St value lies within the transition zone for all the cylinders at Re $\sim$ 200 and 250 with values reaching as high as 0.44.

Figure 24(a) shows the variation of St with rotation rate, α, for the nonhydrophobic cylinder at Re $\sim$ 250 and 200. At Re $\sim$ 200, the Strouhal number shows a weak dependence on α until $\alpha =$ 2 with a general increasing trend. Subsequently, it increases with rotation rate to a maximum of 0.44 near $\alpha = 3$. Thereafter, the Strouhal number decreases with an increase in α. It also appears to suggest from the data that the St trend with Reynolds number looks indefinite. The reason for the disparity in the trend can be attributed to centrifugal instabilities and interaction between the vortex shedding as also alluded to by Diaz *et al.* [4] in the context of wake structure. The variation of St with α is similar to that of rotating cylinder experimental data and computational results reported in the literature [4,14,15] until $\alpha \sim 2$. All the hydrophobic cylinders behave similar to that

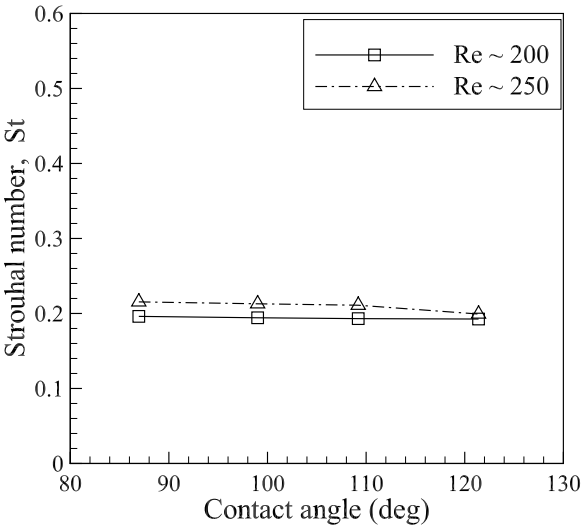

FIG. 25. Strouhal number variation with the level of hydrophobicity of stationary cylinders at Re ∼ 200 and 250.

of the nonhydrophobic cylinder case at least for Strouhal number behavior with the maximum rate of vortex shedding near the transition regime. However, the difference in the maximum Strouhal number obtained at Re ∼ 200 and 250 decreases with increases in slip nature over the surface. The Reynolds number influence over the vortex shedding rate in the transition region remains unresolved due to uncertainties noted in wake structures due to its variable nature. In addition, maximum St values decrease with hydrophobicity at Re ∼ 250 and 200 for hydrophobic cylinders having levels II and III of hydrophobicity.

Figure 25 shows the variation of Strouhal number with the level of hydrophobicity in terms of the contact angle for stationary cylinders. It is observed that as the contact angle of water with the surface increases, Strouhal number appears to decrease slightly at Re ∼ 200 and 250. The observed trend of Strouhal number is similar to the results obtained by Muralidhar *et al.* [17].

The distance between the two vortices of same sign (wavelength) is an important feature that characterizes the wake. The schematic of wavelength measured is shown in Fig. 26. The wavelength was measured at $X/D \sim 14$, 42, and 70 for 3 sec of flow visualization data and then averaged to get the mean value. The variations of Strouhal number and wavelength shown in Figs. 24 and 27, respectively, show that they are negatively correlated with rotation rate for Re ∼ 250 at $X/D \sim 14$.

The wake structure shows an interesting evolution pattern as it develops far downstream. To study far-wake evolution for cylinders with various levels of hydrophobicities, flow visualization was done at downstream distances. Figure 28 shows the evolution of wake up to 84 diameters for nonhydrophobic cylinder at Re ∼ 200. Flow visualization images shown at downstream distances $X \sim 0D$–$28D$, $28D$–$56D$, and $56D$–$84D$ are from different realizations of the experiment. At $\alpha = 0$,

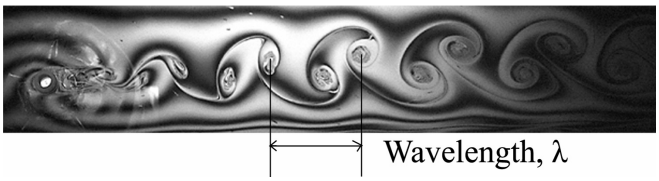

FIG. 26. Illustration of wavelength, λ, measurement.

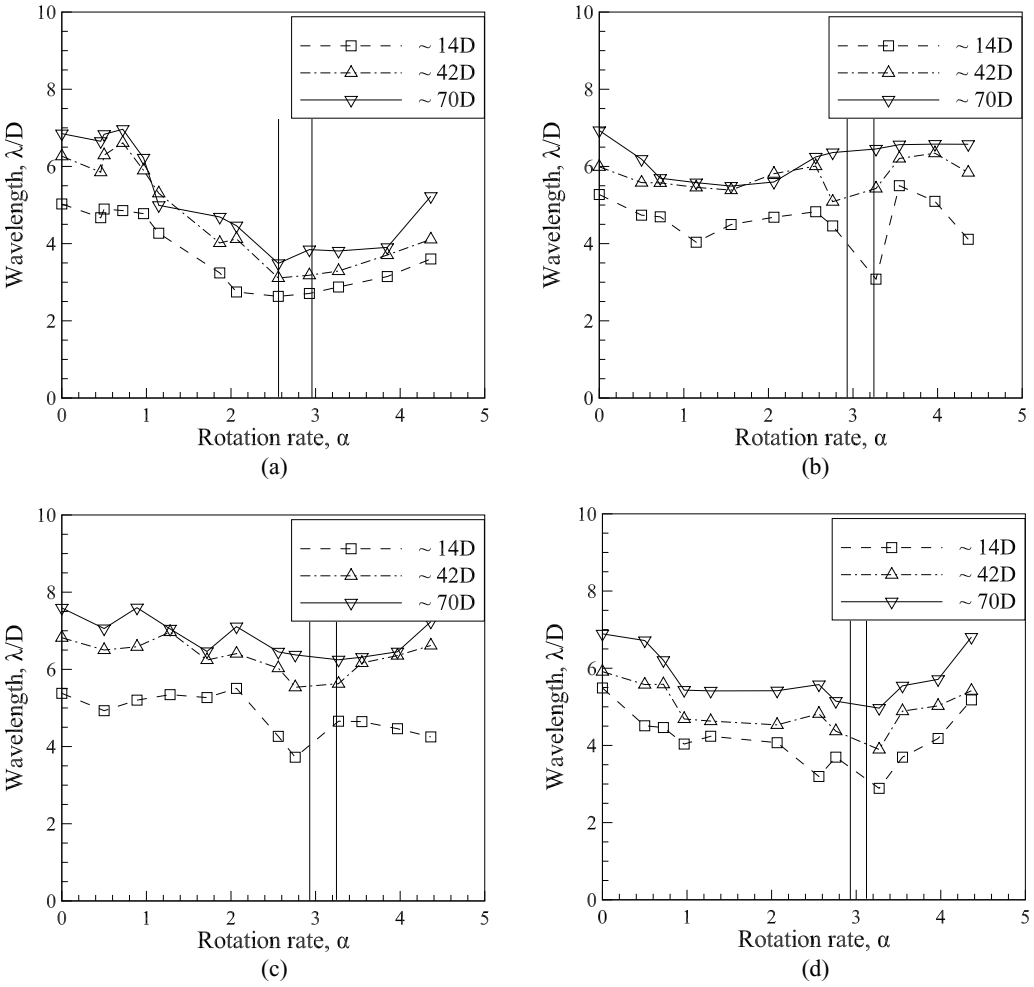

FIG. 27. Normalized wavelength variation with rotation rate at Re $\sim$ 250 for (a) nonhydrophobic cylinder, (b) hydrophobic cylinder of level I, (c) hydrophobic cylinder of level II, and (d) hydrophobic cylinder of level III, with transition zone marked with solid vertical lines.

in the near wake until $X/D \sim 25$, the vortices of opposite sign form a pair such that it is periodic and a fully formed vortex street with vortices being symmetric about the flow axis. As they move farther downstream, for example, from $X \sim 25D$ to $50D$, they gradually deform, and upon reaching $X \sim 85D$ the vortex pairs are elongated and no longer form a symmetric structure. At $X \sim 84D$, the wavelength of the vortex street appears to have increased, and the vortex pairs are stretched in the streamwise direction similar to that reported by Taneda [21]. Additionally, Georgiev *et al.* [23] observed an increase in distance between vortices with downstream distance from his PIV data in a soap film tunnel. As the rotation rate increases to 2.26, it is seen from the flow visualization data that the vortex shedding happens in a way similar to that for $\alpha = 0$ except that the vortices seem to deform closer to the cylinder due to the disparity in the relative velocities over the surface of the cylinder. In the transition zone, a similar wake structure is observed downstream with counterclockwise vortices seen intermittently in the single-signed vortex street. At higher rotation rates until 4.36 after the transition wake morphology, only single-signed vortex street is observed. In the regime from $\alpha = 0$ to 4.36, it is observed that the wavelength of the vortex street increases as the

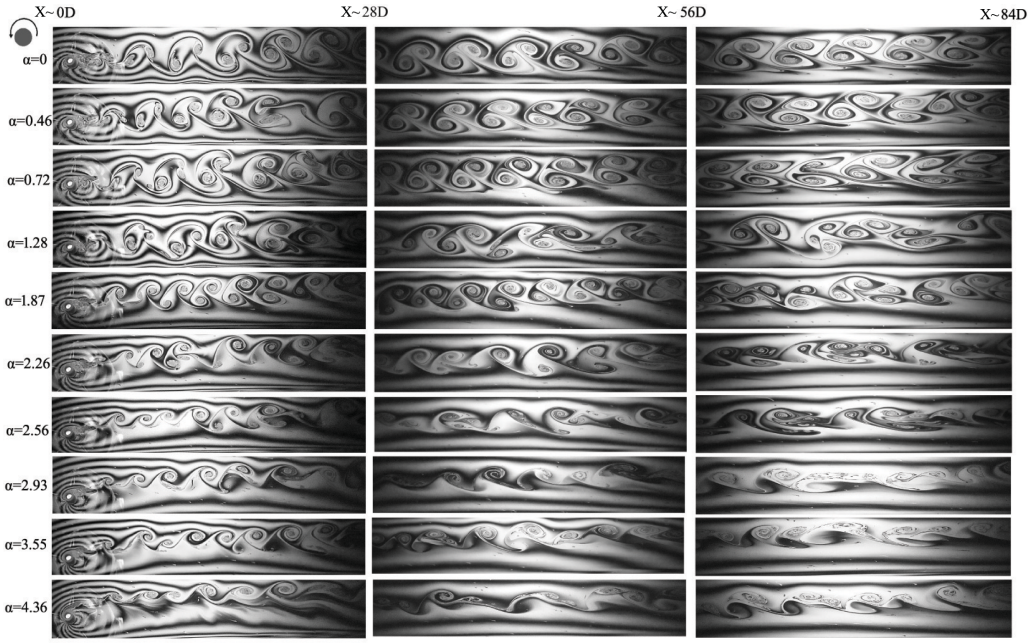

FIG. 28. Downstream wake structures of nonhydrophobic cylinder at various counterclockwise rotation rates at Re $\sim$ 250.

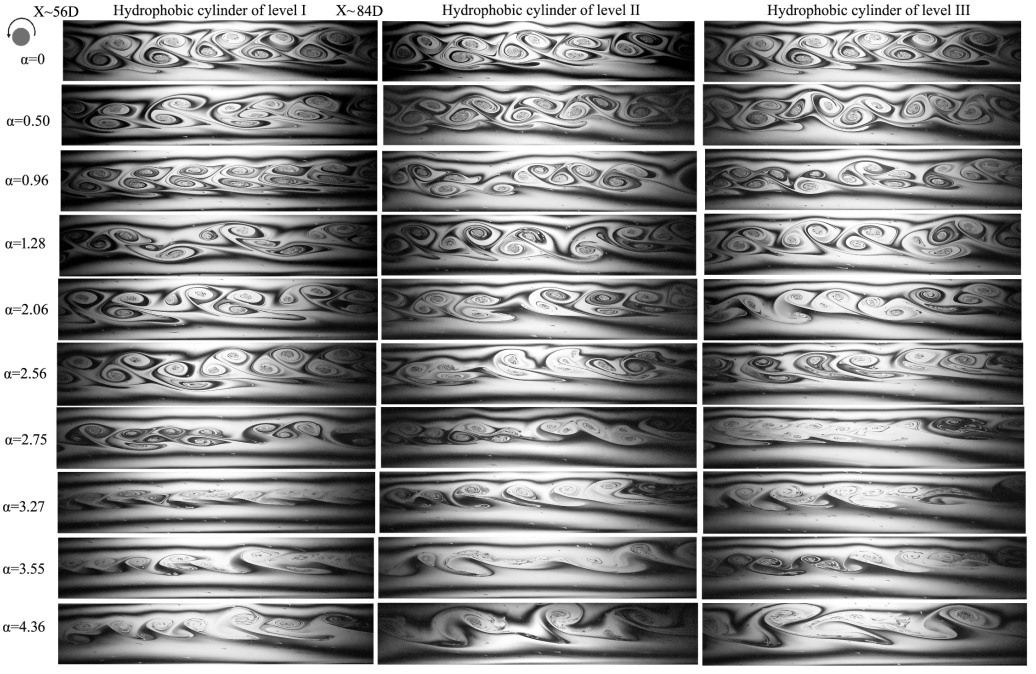

FIG. 29. Downstream wake structure of hydrophobic cylinders at various counterclockwise rotation rates at Re $\sim$ 250, shown at location $X \sim 56D$–$84D$.

TABLE II. Percentage of error in wavelength measurements.

Streamwise distance	$X \sim 14D$	$X \sim 42D$	$X \sim 70D$
Nonhydrophobic cylinder	16.67%	23.64%	22.77%
Hydrophobic cylinder level 1	14.90%	11.03%	11.53%
Hydrophobic cylinder level 2	17.71%	19.49%	20.15%
Hydrophobic cylinder level 3	16.30%	11.65%	14.78%

flow progresses farther downstream. This trend is shown in Fig. 27 for rotating cylinders of different levels of hydrophobicity with α. The size of the vortices increases along the downstream distance, distorting the wake and interacting among themselves. This results in increase in uncertainty in the measurements of wavelength. The percentage error in wavelength measurement at various downstream distances is tabulated in Table II. Visually, far-wake morphology from $X \sim 50D$ to $84D$ does not show any significant changes in wake structure due to surface modification as can be seen in Fig. 29.

IV. SUMMARY AND CONCLUDING REMARKS

Experimental investigation of a rotating cylinder rotating counterclockwise in a flowing soap film at Re $\sim$ 200 and 250 is performed for both hydrophobic and nonhydrophobic cylinders from $\alpha = 0$ to 4.36. Flow visualization and PIV techniques were used in the study of the wake dynamics. The following conclusions can be drawn from the study:

(1) A regime of transition from von Kármán vortex shedding to single-signed vortex shedding was noted with no indication of suppression of vortex shedding.

(2) The ratio of shedding frequency, f_{ccw}/f_{cw}, varies with rotation rate, and it reaches a maximum before the transition zone. The peak value increases with the increase in hydrophobicity levels of the cylinder surface.

(3) Shed clockwise vortices are always stronger than the shed counterclockwise vortices at various rotation rates, α, until the transition zone. In addition, the relative strength of the shed clockwise vortices to counterclockwise vortices increases with α and reaches a maximum at near $\alpha \sim 3$, i.e., the transition zone, for a nonhydrophobic cylinder at Re $\sim$ 250.

(4) Counterclockwise vorticity wraps around the cylinder, increasing its strength around the cylinder with an increase in rotation rate and, in addition, deflects the attached clockwise vorticity upwards weakening its strength around the cylinder.

(5) Location of the stagnation point after it is lifted off the surface is observed to be in the windward direction at $\sim$135° at $\alpha \sim 3.85$ for Re $\sim$ 250.

(6) The transition regime occurred in the range of a normalized rotation rate greater than 2 for both hydrophobic and nonhydrophobic cylinders at Re $\sim$ 200 and 250.

(7) The sign of vortices in a single-signed vortex street is in an opposite sense to the rotation of the rotating cylinder.

(8) Influence of the Reynolds number and hydrophobicity was observed on the onset of the transition regime.

(9) In the transition regime, the rate of the detachment of eddies was a maximum for both hydrophobic and nonhydrophobic cylinders irrespective of flow conditions, i.e., Reynolds number.

(10) In general, the trend of St with rotation rate was observed to be increasing till the transition zone and then it gradually decreases.

(11) A far-wake study showed a significant distortion in the wake structure observed in the range $X/D \sim$50 to 84, which occurred due to the elongation of the vortex pair for both hydrophobic and nonhydrophobic cylinders.

ACKNOWLEDGMENTS

The authors would like to acknowledge the help provided by the Imagineering laboratory, IIT Kanpur, in fabricating the hydrophobic cylinders. We express sincere gratitude to Prof. Kamal Poddar, Low Speed Aerodynamics laboratory, for providing PIV equipment for experiments and G. Balamurugan (a Ph.D. student) for help with PIV experiments.

[1] L. Prandtl, Magnuseffekt und Windkraftschiff, Naturwissenschaften **13**, 93 (1925).
[2] M. Glauert, The flow past a rapidly rotating circular cylinder, Proc. R. Soc. Lond. A **242**, 108 (1957).
[3] P. Tokumaru and P. Dimotakis, The lift of a cylinder executing rotary motions in a uniform flow, J. Fluid Mech. **255**, 1 (1993).
[4] F. Diaz, J. Gavalda, J. G. Kawall, J. G. Keffer, and F. Giralt, Vortex shedding from a spinning cylinder, Phys. Fluids **26**, 3454 (1983).
[5] V. Modi, Moving surface boundary-layer control: A review, J. Fluids Struct. **11**, 627 (1997).
[6] M. Coutanceau and C. Menard, Influence of rotation on the near-wake development behind an impulsively started circular cylinder, J. Fluid Mech. **158**, 399 (1985).
[7] H. Badr and S. Dennis, Time-dependent viscous flow past an impulsively started rotating and translating circular cylinder, J. Fluid Mech. **158**, 447 (1985).
[8] H. Badr, M. Coutanceau, S. Dennis, and C. Menard, Unsteady flow past a rotating circular cylinder at Reynolds numbers 10^3 and 10^4, J. Fluid Mech. **220**, 459 (1990).
[9] Y.-M. Chen, Y.-R. Ou, and A. J. Pearlstein, Development of the wake behind a circular cylinder impulsively started into rotatory and rectilinear motion, J. Fluid Mech. **253**, 449 (1993).
[10] S. Mittal and B. Kumar, Flow past a rotating cylinder, J. Fluid Mech. **476**, 303 (2003).
[11] S. Kumar, C. Cantu, and B. Gonzalez, Flow past a rotating cylinder at low and high rotation rates, J. Fluids Eng. **133**, 041201 (2011).
[12] Y. Chew, M. Cheng, and S. Luo, A numerical study of flow past a rotating circular cylinder using a hybrid vortex scheme, J. Fluid Mech. **299**, 35 (1995).
[13] S. Kang, H. Choi, and S. Lee, Laminar flow past a rotating circular cylinder, Phys. Fluids **11**, 3312 (1999).
[14] T. Kimura, M. Tsutahara, and Z.-Y. Wang, Wake of a rotating circular cylinder, AIAA J. **30**, 555 (1992).
[15] J. F. Jaminet and C.W. Van Atta, Experiments on vortex shedding from rotating circular cylinders, AIAA J. **7**, 1817 (1969).
[16] G.-H. Hu, D.-J. Sun, X.-Y. Yin, and B.-G. Tong, Hopf bifurcation in wakes behind a rotating and translating circular cylinder, Phys. Fluids **8**, 1972 (1996).
[17] P. Muralidhar, N. Ferrer, R. Daniello, and J. P. Rothstein, Influence of slip on the flow past superhydrophobic circular cylinders, J. Fluid Mech. **680**, 459 (2011).
[18] T. Min and J. Kim, Effects of hydrophobic surface on skin-friction drag, Phys. Fluids **16**, L55 (2004).
[19] D. You and P. Moin, Effects of hydrophobic surfaces on the drag and lift of a circular cylinder, Phys. Fluids **19**, 081701 (2007).
[20] Q. Ren, Y. L. Xiong, D. Yang, and J. Duan, Flow past a rotating circular cylinder with superhydrophobic surfaces, Acta Mech. **229**, 3613 (2018).
[21] S. Taneda, Downstream development of the wakes behind cylinders, J. Phys. Soc. Jpn. **14**, 843 (1959).
[22] O. Inoue and T. Yamazaki, Secondary vortex streets in two-dimensional cylinder wakes, Fluid Dyn. Res. **25**, 1 (1999).
[23] P. Vorobieff, D. Georgiev, and M. S. Ingber, Onset of the second wake: Dependence on the Reynolds number, Phys. Fluids **14**, L53 (2002).
[24] M. Rutgers, X. Wu, and W. Daniel, Conducting fluid dynamics experiments with vertically falling soap films, Rev. Sci. Instrum. **72**, 3025 (2001).
[25] M. Gharib and P. Derango, A liquid film (soap film) tunnel to study two-dimensional laminar and turbulent shear flows, Physica D **37**, 406 (1989).

[26] A. Roshko, On the development of turbulent wakes from vortex streets technical note 2913, National Advisory Committee for Aeronautics, 1954.
[27] Y. Couder, J. Chomaz, and M. Rabaud, On the hydrodynamics of soap films, Physica D **37**, 384 (1989).
[28] M. Rivera, P. Vorobieff, and R. E. Ecke, Turbulence in Flowing Soap Films: Velocity, Vorticity, and Thickness Fields, Phys. Rev. Lett. **81**, 1417 (1998).
[29] D. Georgiev and P. Vorobieff, The slowest soap-film tunnel in the southwest, Rev. Sci. Instrum. **73**, 1177 (2002).
[30] W. Thielicke and E. Stamhuis, PIVlab—Towards user-friendly, affordable and accurate digital particle image velocimetry in MATLAB, J. Open Res. Softw. **2**, 1 (2014).
[31] T. Schnipper, A. P. Andersen, T. Bohr, J. N. Sørensen, and H. Aref, Exotic wakes of flapping fins, PhD. dissertation, Department of Physics and Center for Fluid Dynamics, Technical University of Denmark, 2011.
[32] A. Andersen, T. Bohr, T. Schnipper, and J. H. Walther, Wake structure and thrust generation of a flapping foil in two-dimensional flow, J. Fluid Mech. **812**, R4 (2017).
[33] C. H. K. Williamson, 2-D and 3-D aspects of the wake of a cylinder, and their relation to wake computations, Lect. Appl. Maths., Am. Math. Soc. **28**, 719 (1991).